ACS OMEGA

Open Access

http://pubs.acs.org/journal/acsodf

Article

Atomic-Scale Insights into the Phase Behavior of Carbon Dioxide and Water from 313 to 573 K and 8 to 30 MPa

Published as part of ACS Omega virtual special issue "CO_2 Geostorage".

Masashige Shiga,* Tetsuya Morishita,* Naoki Nishiyama, Masao Sorai, Masaatsu Aichi, and Ayaka Abe

Cite This: *ACS Omega* 2024, 9, 20976−20987

Read Online

ACCESS | Metrics & More | Article Recommendations | Supporting Information

ABSTRACT: We performed molecular dynamics (MD) simulations of CO_2 + H_2O systems by employing widely used force fields (EPM2, TraPPE, and PPL models for CO_2; SPC/E and TIP4P/2005 models for H_2O). The phase behavior observed in our MD simulations is consistent with the coexistence lines obtained from previous experiments and SAFT-based theoretical models for the equations of state. Our structural analysis reveals a pronounced correlation between phase transitions and the structural orderliness. Specifically, the coordination number of Ow (oxygen in H_2O) around other Ow significantly correlates with phase changes. In contrast, coordination numbers pertaining to the CO_2 molecules show less sensitivity to the thermodynamic state of the system. Furthermore, our data indicate that a predominant number of H_2O molecules exist as monomers without forming hydrogen bonds, particularly in a CO_2-rich mixture, signaling a breakdown in the hydrogen bond network's orderliness, as evidenced by a marked decrease in tetrahedrality. These insights are crucial for a deeper atomic-level understanding of phase behaviors, contributing to the well-grounded design of CO_2 injection under high-pressure and high-temperature conditions, where an atomic-scale perspective of the phase behavior is still lacking.

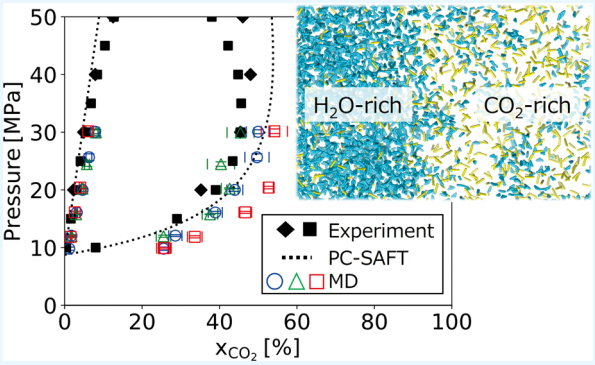

1. INTRODUCTION

CCUS (carbon capture, utilization, and storage) has been considered one of the most practical and effective options for achieving sustainable energy development by meeting the increasing energy demand while reducing the amount of carbon dioxide (CO_2) emissions into the atmosphere.[1−3] The CO_2-enhanced geothermal system (CO_2-EGS), an innovative concept first proposed by Brown,[4] utilizes CO_2 instead of water as a transfer fluid in geothermal energy production. This approach has been gaining strong attention because CO_2 offers several advantages as a working fluid in terms of compressibility,[5] mobility,[6,7] and capability of efficient fracturing.[7−9] In addition to the benefit for geothermal production, there are considered additional advantages in terms of storing unrecovered CO_2 underground[6,10−12] as well as the problem of water scarcity.[5]

Given the potential advantages of CO_2 utilization for EGS, there has been extensive research on the impact of CO_2 utilization in geothermal reservoir rocks.[5,6,10−14] Most of these studies have considered the single phase of CO_2, aiming at injection to hot dry rock (HDR) while there are also investigations into hydrothermal reservoirs, which contain water (H_2O).[15,16] In terms of CO_2-EGS in hydrothermal reservoirs, it is necessary to consider the flow of the CO_2 + H_2O system.[15,16] Moreover, even for CO_2-EGS in HDR, the working fluid would become water-dissolved CO_2;[7] therefore, it is significant to consider the impact of the water content on the phase behavior and properties of CO_2 in geothermal reservoirs.

Regarding the phase behavior of CO_2 and water at geothermal temperature conditions, Tödheide and Franck (1963) and Takenouchi and Kennedy (1964) reported data at temperatures above 500 K.[17,18] At temperatures exceeding 500 K, a significant shift in the coexistence curve (as depicted in the $P-x$ diagram in Figure 3 in Section 3.1) is observed with respect to the temperature, indicating that CO_2 and water are miscible across a broader range of CO_2 mole fractions. For example, at a constant pressure of 30 MPa, the phase coexistence occurs at a CO_2 mole fraction of approximately 60% when the temperature is 543 K. Conversely, at the same pressure but at a temperature of 573 K, the phase coexistence occurs at a CO_2 mole fraction of 45%.[17,18] This implies that

Received: January 4, 2024
Revised: March 17, 2024
Accepted: April 10, 2024
Published: May 3, 2024

phase behavior would be sensitively changed in geological reservoirs for CO_2-EGS. In terms of modeling the phase behavior, the equation of state (EOS) can well reproduce the experimental data of coexistence lines up to pressure conditions of approximately 50 MPa [see calculation results by simplified cubic plus associating (sCPA) EOS (Soave−Redlich−Kwong and Peng−Robinson),[19] PC-SAFT EOS,[20] and SAFT-VR Mie EOS[21] shown in Section 3.1]. EOS have been sophisticated through implementing intermolecular interactions and successfully employed in modeling thermodynamic properties of CO_2-bearing fluids (e.g., refs 22 and 23).

Microscopic insights have provided not only a higher accuracy for prediction but also a deeper understanding of macroscopic phase behavior. Molecular dynamics (MD) simulations have uncovered the mechanism behind the CO_2−H_2O IFT (interfacial tension) changes by utilizing descriptors of the molecular arrangement—such as the number of hydrogen bonds and the orientation angle of molecules—in the interfacial region and the bulk region.[24−29] Structural information at the microscopic level, including radial distribution function (RDF), is closely related to transport properties (e.g., refs 30−32), and it has been applied for estimation and interpretation of dynamical properties; the viscosity of supercritical water formulated as a function of the number of hydrogen bonds[33] and diffusivity of supercritical CO_2 formulated based on RDF.[34] Furthermore, molecular-scale perspective has contributed to developing machine learning-based models to estimate the IFT.[35] As illustrated in these examples, a better description of CO_2 + H_2O systems from atomic-scale perspective would improve the modeling and interpretation of fundamental properties of CCUS.

While spectroscopic experiments[36,37] and molecular simulations[29,38−41] on CO_2 + H_2O systems have been performed at high-temperature and high-pressure conditions, there is still a lack of an atomic-level understanding in structural changes in molecular assemblies associated with phase transitions. Beyond conventional conditions for CGS—specifically, temperatures ranging from 300 to 350 K and pressures around 10 MPa, representative of a depth of 1 km—molecular simulation efforts have predominantly focused on the improvement of force fields (e.g., refs 38−41). These studies, while valuable, have not illuminated the variations in the molecular arrangement associated with phase transition. The experimental challenge of directly observing the phase behavior under high-temperature conditions further limits our comprehension. In this study, therefore, we perform MD simulations at temperature from 313 to 573 K, which includes a promising reservoir condition for CGS, CO_2-EGS, and CO_2-plume geothermal (CPG) technology.

This paper is organized as follows: simulation methods and parameters are introduced in Section 2. In Section 3.1, we demonstrate that the P−x diagram computed in our MD simulations is in good agreement with previously reported experimental data. Sections 3.2, 3.3, and 3.4 include our new findings from detailed analyses in the molecular arrangement.

2. MATERIALS AND METHODS

2.1. Simulation Systems. To obtain coexistent lines of CO_2 + H_2O systems, we used the direct coexistent (DC) method which has been demonstrated as a promising way to obtain phase equilibria,[42−45] while it requires relatively higher computational cost than the Gibbs ensemble Monte Carlo (GEMC) method,[46] another common way. The solubility of CO_2 in the water-rich phase and that of water in the CO_2-rich phase were estimated using the slab system (Figure 1a), where

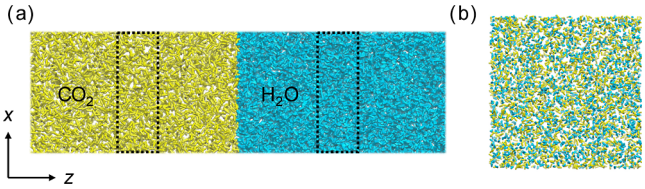

Figure 1. Snapshots of simulation systems under initial conditions: (a) slab system for DC calculations and (b) cubic system for the structural analysis. CO_2 and H_2O molecules are colored yellow and blue, respectively. Note that a periodic boundary condition was employed. The dotted lines in (a) indicate the bulk region for the calculation of the solubility.

the total number of molecules was determined in preparing the initial configuration so that the CO_2-rich phase and water-rich phase were clearly separated and the interface stably formed in equilibrium. The dotted lines in Figure 1 indicate the bulk region, where the number of molecules is counted and subsequently averaged over the production run to estimate the solubility. In this analysis, the regions 1 nm from the center of mass, with a thickness of 2 nm, in both water-rich and the CO_2-rich phases were considered as the bulk region for each phase. Altering the thickness to 3 or 4 nm did not yield any significant changes in the computed solubility values.

The statistical uncertainties associated with the solubility in both bulk phases were estimated by partitioning the production runs into 40 blocks, each encompassing a 1 ns interval (see computational time mentioned in Section 2.3). The standard deviations of these block averages were subsequently calculated, providing an estimate of the uncertainty of the solubility. MD simulations of such two-phase interfacial systems have been performed in numerous preceding studies.[26,29,48] However, the majority of these were aimed at evaluation of the IFT at temperatures below 400 K. To the best of our knowledge, there exists no prior DC calculation aimed at determining the phase boundaries under high-temperature conditions above 400 K.

To analyze the molecular arrangement of the CO_2 + H_2O systems under phase-separated and mixed states, we employed cubic systems with various proportions of CO_2 and H_2O molecules (Figure 1b). The merits of employing a cubic system include the ease of analysis. The initial structure was prepared by randomly arranging the molecules in the box. Note that the analysis conducted along the coexistence line of the CO_2−water system utilized data obtained from the DC calculations.

Temperature conditions include 313, 373, 473, 543, and 573 K. Pressure conditions for the DC method are 8, 10, 12, 16, 20, 25, and 30 MPa while those for the structural analysis are 10 and 30 MPa. The total number of molecules for the DC calculations is shown in Table S1 while that for the cubic systems was set to 4800. Computations under a different molar ratio of CO_2, defined as x_{CO_2}, from 0 to 100% were performed for each temperature and pressure condition. Note that reservoir conditions for the CO_2-EGS project by JOGMEC (Japan Organization for Metals and Energy Security) would include temperature and pressures up to 573 K and 20 MPa.

2.2. Force Fields. In classical molecular simulations, the EPM2[49] and TraPPE[50] are often utilized for CO_2, while the SPC/E[51] and TIP4P/2005[52] are employed for H_2O. The

https://doi.org/10.1021/acsomega.4c00133
ACS Omega 2024, 9, 20976−20987

Table 1. Procedures and Ensembles Utilized for Slab and Cubic Systems

	equilibration[a]	production
Slab systems	$NP_{zz}AT$: (1) Berendsen barostat + Berendsen thermostat[59] for 20 ns (2) Parrinello−Rahman barostat[60]+ Nosé−Hoover thermostat for 50 ns; *NVT*: Nosé−Hoover thermostat for 10 ns	*NVT*: Nosé−Hoover thermostat for 40 ns
Cubic systems	*NPT*: (1) Berendsen barostat + Berendsen thermostat for 50 ns (2) Parrinello−Rahman barostat + Nosé−Hoover thermostat for 30 ns; *NVT*: Nosé−Hoover thermostat for 30 ns	*NVT*: Nosé−Hoover thermostat for 40 ns

[a]In the *NPT* and $NP_{zz}AT$ calculations, the Berendsen barostat and thermostat (the time constants τ_p and τ_T are 5.0 and 0.2 ps, respectively) were firstly used for equilibration and then they were switched to the Parrinello−Rahman barostat (the time constant τ_p is 5.0 ps) and Nosé−Hoover thermostat, respectively, for the remaining duration of the *NPT* runs.

nonbonded interatomic interactions of these force fields are described by the Lennard-Jones (LJ) potential and the Coulomb potential, as shown in eq 1, where ε_{ij} and σ_{ij} are the energy and size parameters of the LJ potential, respectively; r_{ij}, q_i, q_j, and ε_0 are the distance between atom i and j, the charge of the particle i, the charge of the particle j, and the dielectric permittivity at vacuum condition, respectively

$$U(r_{ij}) = 4\varepsilon_{ij}\left[\left(\frac{\varepsilon_{ij}}{r_{ij}}\right)^{12} - \left(\frac{\sigma_{ij}}{r_{ij}}\right)^{6}\right] + \frac{1}{4\pi\varepsilon_0}\sum_{i\neq j}\frac{q_i q_j}{r_{ij}} \quad (1)$$

In this study, we employed five pairs of force fields for CO_2 and H_2O molecules: (A) the EPM2 + SPC/E[51] models with reoptimization by Vlcek et al. (2011),[39] (B) the TraPPE + SPC/E models, (C) the TraPPE + TIP4P/2005 models, (D) EPM2 + SPC/E models, and (E) PPL[53] + SPC/E models. The first three combinations show a good performance in our recent study[29] as well as other previous reports[26,47] in terms of CO_2 solubility in water and the IFT of CO_2 + H_2O systems. To discuss the dependency on force field parameters, (D) and (E) were additionally employed, which give a less accurate CO_2 solubility in water as demonstrated in our previous study.[29] (D) is the unmodified version of (A), and (E) has the largest ε_{ij} value among the five models. For the LJ parameters of unlike atoms, the Lorentz−Berthelot rules were employed for (B), (C), and (D). For (A), modifications by Vlcek et al. (2011) were applied, while for (E), parametrization by Patterson and Lynden-Bell (1998)[53] was utilized. ε_{ij} values of these five models are summarized in Table S2.

The cutoff radius was 1.1 nm for both LJ potential and the short-range part of the Coulomb potential. The long-range part of the Coulomb potential was treated with the particle mesh Ewald (PME) method. The long-range dispersion corrections for the LJ potential were applied. The bonded terms of all models were treated as rigid using the LINear Constraint Solver (LINCS)[54] algorithm. We used GROMACS 2019[55] for conducting the MD simulations and VMD (version 1.9.4)[56] for visualizing the snapshots.

2.3. Simulation Process. The simulation process, involving equilibration to stabilize the system followed by production runs, consists of equilibration and production runs, and it is summarized in Table 1. For the slab system, we conducted *NVT* calculations (the number of particles N, the total volume V, and temperature T were maintained at constant values) after $NP_{zz}AT$ calculations (the number of particles N, the pressure in the z-direction P_{zz}, the surface area A, and temperature T were maintained at constant values) using the DC method. For the cubic system, we performed *NVT* calculations after isotropic *NPT* calculations for the structural analyses. The last 40 ns (4.0×10^7 steps) of the production run performed by using the Nosé−Hoover thermostat[57,58] (the time constant τ_T = 0.2 ps) was employed to estimate the physical properties. We regarded the system as in the equilibrium state after the potential energy, pressure, and density were converged. Time variations of P_{zz} and x_{CO_2} in the CO_2-rich phase of the model (A) in the production run of DC calculations are shown in Figures S1 and S2, respectively. Box sizes for the production runs are shown in Tables S3 and S4. It should be noted that the pressure values for the phase boundaries, as plotted in the $P-x$ diagram, were estimated in the *NVT* simulation. These pressure values are almost coincident with those obtained from both $NP_{zz}AT$ and *NPT* simulations used for equilibration purposes, as depicted in Figures S1 and 3 (pertaining to DC calculation) and detailed in Table S5 (which addresses structural analysis).

2.4. Descriptors of the Molecular Arrangement.

2.4.1. Coordination Number. Coordination number (CN) is the number of neighboring atoms with respect to a central atom, as shown in Figure 2a. It is computed by integrating

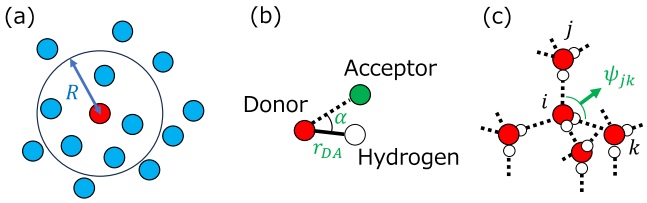

Figure 2. Schematic images of definitions of descriptors for molecular arrangement: (a) CN is evaluated by integration of RDF (the blue balls within the distance R from the red ball are counted), (b) hydrogen bond is counted when r_{DA} is less than 0.35 nm and the angle α is less than 30°, and (c) tetrahedrality is computed from ψ_{jk}, which is defined from one oxygen atom of H_2O molecules and its four nearest neighbors (eq 2).

RDF up to the cutoff distance R. CN is considered as a suitable descriptor for examining structural changes because previous MD simulation studies have shown that CN exhibits a clear correlation with phase transitions.[61] We estimated CN with two radii R (0.3 and 0.5 nm), which correspond to the first peaks of RDF of Ow (oxygen of H_2O)−Ow and C (carbon of CO_2)−C, respectively. For the sake of simplicity, "CN (A−B)" and "CN of A−B" denote the CN of B around A (A is the central atom). Note that we validated our calculation procedure for CN by estimating CN (C−C) in pure CO_2 and CN (Ow−Ow) in pure water. As shown in Figures S3 and S4, RDFs are in good agreement with the trend against temperature reported by previous studies.[62]

2.4.2. Number of Hydrogen Bonds per H_2O Molecule. As one of the descriptors characterizing the structural properties of water, the number of hydrogen bonds per water molecule, n_{HB}, has been frequently used in previous studies.[62] The method for counting hydrogen bonds was based on the approach by Luzar and Chandler (1996).[63] As shown in Figure

https://doi.org/10.1021/acsomega.4c00133
ACS Omega 2024, 9, 20976−20987

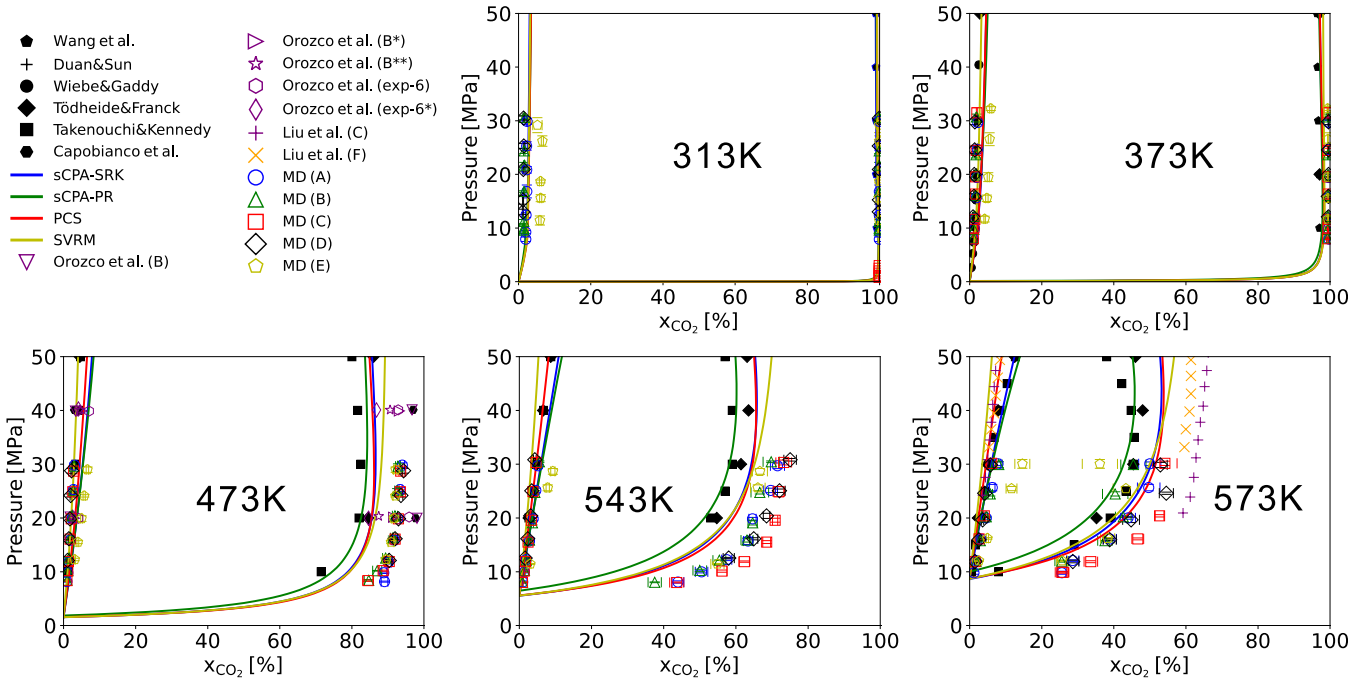

Figure 3. $P-x$ diagram: The legend is shown in the top left; experimental data (Wang et al.,[65] Wiebe and Gaddy,[66] Tödheide and Franck,[17] Takenouchi and Kennedy,[18] and Capobianco et al.[67]) and the experimental-based model (Duan and Sun[68]) are plotted. "sCPA-SRK", "sCPA-PR", "PCS", and "SVRM" are calculation data of sCPA (Soave−Redlich−Kwong), sCPA (Peng−Robinson), PC-SAFT, and SAFT-VR-Mie EOS. The results of the current study by the DC method are plotted for different force field combinations: (A) EPM2 + SPC/E reoptimized by Vlcek et al.,[39] (B) TraPPE + SPC/E, (C) TraPPE + TIP4P/2005, (D) EPM2 + SPC/E, and (E) PPL + SPC/E. GEMC simulation results by Orozco et al. are also presented in the $P-x$ diagram, which employed the following five models: B, B*, B**, exp-6, and exp-6* denote the model (B), (B) with an optimized LJ parameter, (B) with optimized charges, the exp-6 model[40] with the Lorentz−Berthelot rule, and the exp-6 model with the parameter optimization, respectively. Liu et al. (C) and Liu et al. (F) denote the results of GEMC simulations by using the model (C) and another model (F) (EPM2 + TIP4P/2005), respectively.[38]

2b, a hydrogen bond is counted when the distance between a donor (D) and an acceptor (A), r_{DA}, is less than 0.35 nm, and the angle of A-D-H (α in Figure 2b) is less than 30°. This method is consistent with the evaluation method used in the GROMACS analysis command "gmx hbond".[55]

2.4.3. Tetrahedrality. Tetrahedrality has been used as a measure of structural orderliness in water and silicon.[30,64] An order parameter q_t, shown in eq 2, ranges from −3 to 1; q_t equals 1 in a perfectly tetrahedral arrangement, while it is zero in a random structure (i.e., ideal gas). The angle ψ_{jk} is defined as shown in Figure 2 (c) and q_t was calculated for all oxygen atoms of water

$$q_t = 1 - \frac{3}{8}\sum_{j=1}^{3}\sum_{k=j+1}^{4}\left(\cos\psi_{jk} + \frac{1}{3}\right)^2 \quad (2)$$

3. RESULTS AND DISCUSSION

3.1. Phase Behavior Computed by the DC Method and Snapshots. Coexistence lines computed by the DC method are shown in Figure 3 with experimental data (Wang et al.,[65] Wiebe and Gaddy,[66] Tödheide and Franck,[17] Takenouchi and Kennedy,[18] and Capobianco et al.[67]), a well-known experiment-based model by Duan and Sun,[68] and the SAFT-type EOS (sCPA (Soave−Redlich−Kwong and Peng−Robinson),[19] PC-SAFT EOS,[20] and SAFT-VR Mie EOS[21]). Note that the coexistence line by the EOS model was calculated by using Clapeyron.jl[69] and the parameters of the EOS model are listed on its GitHub page.

Our MD results are in good agreement with the previous experimental data. At 313, 373, and 473 K, the results are comparable, except for (E). The model (E) has the largest attractive energy ε_{ij}, which would result in an overestimation of CO_2 solubility in water. Comparing the other four models, from the perspective of reproducibility of experimental values at 543 and 573 K, (A,B) especially works well, and these are thus promising molecular models to study CO_2−water and CO_2−water−rock systems under conditions for CGS and CO_2-EGS. (A) and (B) are considered as reasonable choices also because many force fields have been developed to be compatible with the SPC-based water model (i.e., the CLAYFF model[70] for clay minerals). Some studies reported that TIP4P/2005 is better in terms of reproducibility of several properties of pure water (i.e., surface tension[71] and diffusivity[72]); therefore, the model (C) would be another plausible option while (C) slightly overestimates the water solubility in CO_2 compared to (A) and (B). On the basis of our previous study, model (A) is the best in terms of not only the water solubility in CO_2 but also the IFT; therefore, we chose model (A) for analyses in Sections 3.2, 3.3, and 3.4. x_{CO_2} at the coexistence line for the CO_2-rich side and that for the water-rich side obtained by the model (A) are summarized in Tables 2 and 3, respectively.

As shown in Figure 4, snapshots of the systems seem to be consistent with the $P-x$ diagram (Figure 3) obtained by experiments, the EOS models, and our DC calculations. These visualize the strong impact of temperature, pressure, and mole fractions on the phase behavior in particular under conditions for CO_2-EGS. At 313 and 373 K, temperatures pertinent to

https://doi.org/10.1021/acsomega.4c00133
ACS Omega 2024, 9, 20976−20987

Table 2. x_{CO_2} at the Coexistence Line for the CO_2-Rich Side (Defined as Δx_{CO_2} = 0%)

	10 MPa	30 MPa
313 K	99.9	99.9
373 K	99.5	99.6
473 K	88.8	93.4
543 K	50.5	71.5
573 K	25.6	50.0

Table 3. x_{CO_2} at the Coexistence Line for the Water-Rich Side

	10 MPa	30 MPa
313 K	2.0	2.3
373 K	1.3	2.2
473 K	1.2	3.0
543 K	1.4	5.1
573 K	1.2	7.9

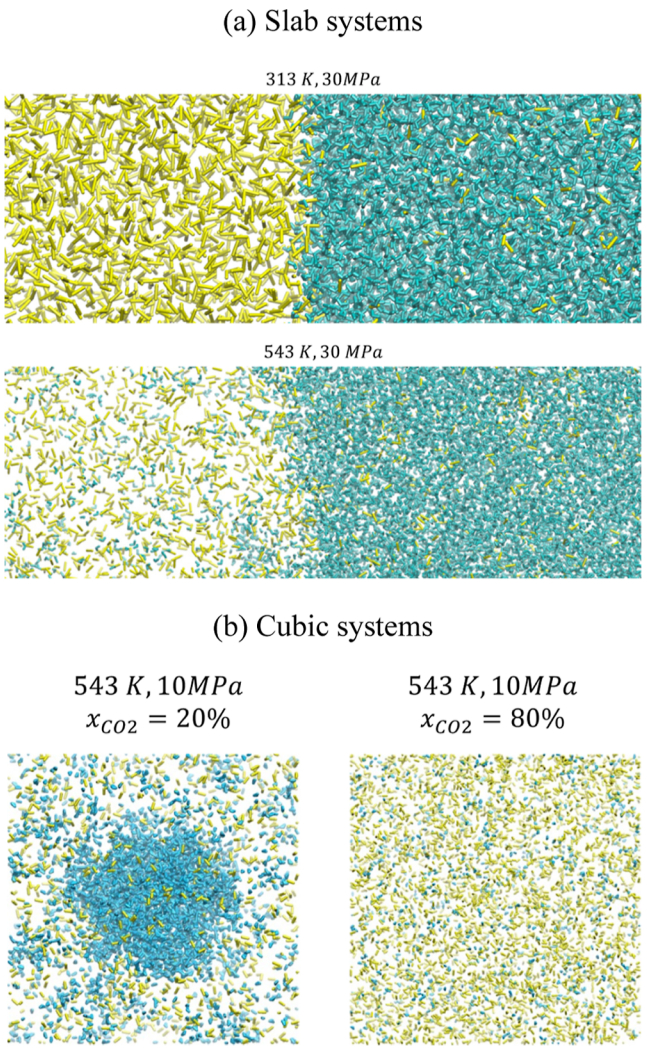

Figure 4. Snapshots of (a) slab systems at 313 and 543 K at 30 MPa and (b) cubic systems for x_{CO_2} = 20 and 80% at 543 K and 10 MPa. These snapshots were obtained using force fields (A). CO_2 and H_2O molecules are colored yellow and blue, respectively. Snapshots are scaled for easy comparison.

conventional CCUS projects, CO_2, and water are phase-separated with x_{CO_2} values ranging from 10 to 90%. Particularly at 313 K shown in Figure 4a, the dissolution of water into the CO_2 phase is nearly invisible. By further increase of the temperature, as illustrated in Figure 4a, the presence of H_2O molecules in the CO_2 phase notably increases. The solubility of water in the CO_2 phase increases significantly with temperature, indicative of enhanced miscibility within this binary system, as presented in Figure 4a,b. This is consistent with the results of the $P-x$ diagram that suggest increased mixing across a broader range of mole fractions. Moreover, snapshots from the slab system illustrate changes in the interface structure; a decrease in the IFT by increasing the temperature is relevant to a thicker interface and decreased structural integrity.[29]

As also plotted in Figure 3, at 473 K, our simulations reproduced experimental data better than previous molecular simulation studies using the same force fields (B), (C), and similar combinations (F) (EPM2 + TIP4P/2005).[40] The accuracy of our results is comparable to those using similarly optimized models.[40] At 573 K where the literature data is even more scarce, our results using (A), (B), and (C) are more accurate than the previous results;[38] furthermore, even though the force fields we used are rigid models, the accuracy is comparable to the results by polarizable models reported in a subsequent paper[41] by the same research group as Liu et al. (2011).[38] This is probably because a longer simulation time both for equilibration and production was employed in this study. Although the DC method would require a higher computational cost compared to the GEMC calculation for obtaining $P-x$ diagrams,[46] our results have demonstrated that the DC method is a reasonable choice even in cases like this study where a multitude of conditions and models are considered.

In the domain of CO_2-EGS, the temperature and pressure conditions explored in this study are primarily targeted. Consequently, such phase behavior is a crucial phenomenon to take into consideration in estimating and optimizing the fluid flow associated with a CO_2 injection. From our previous MD simulations,[29] it has been inferred that upon exceeding 500 K, the IFT decreases by approximately 80% compared to those at conventional CGS reservoir conditions (i.e., 313 K and 10 MPa at 1 km depth), suggesting a significant reduction in the capillary pressure that is a key driving force of the two-phase fluid flow in porous and fractured rock systems.[73,74] Additionally, as demonstrated by the present results, under high-temperature conditions, CO_2 and water are mixed over a wide range of molar ratios, leading to the disappearance of phase interfaces, which is another significant aspect from the perspective of the driving forces. Furthermore, even under phase-separating conditions, there exists a potential for flow in the form of small droplets or bubbles, as depicted in the snapshots (Figure 4b).

Overall, our MD simulations well reproduce the phase behavior of CO_2 + H_2O systems at conditions for CGS and CO_2-EGS. Furthermore, the use of detailed visualizations through snapshots provides a more intuitive understanding of the complex phase behavior. On the basis of these findings, in the following sections, we delve into the molecular arrangement in line with phase transition.

3.2. Coordination Number. Distribution of CN at each pressure and temperature condition is shown in Figures 5 and S5−S11. Data calculated for R = 0.3 nm are plotted in Figures

https://doi.org/10.1021/acsomega.4c00133
ACS Omega 2024, 9, 20976−20987

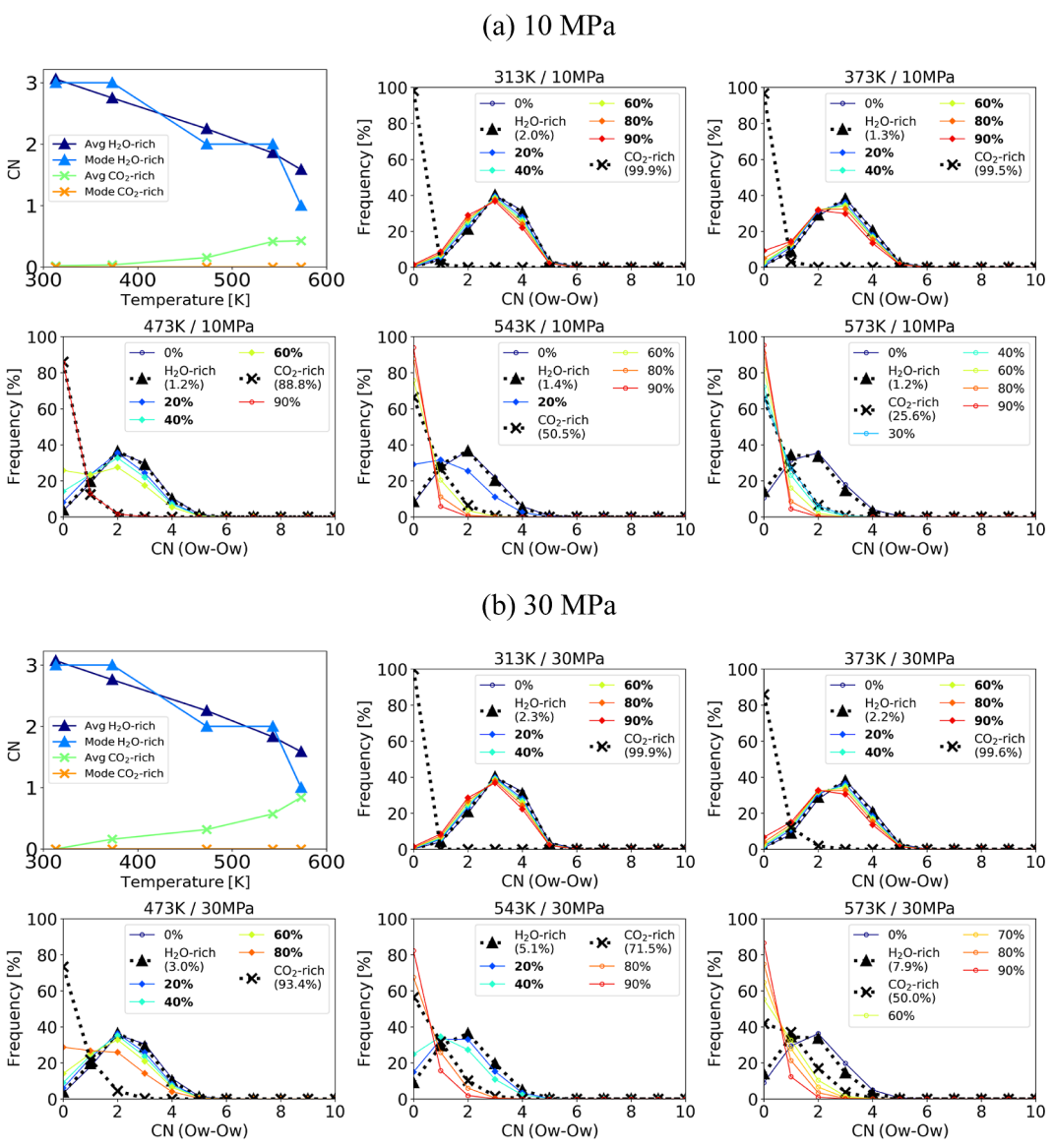

Figure 5. Coordination number of Ow−Ow (R < 0.3 nm) at (a) 10 and (b) 30 MPa; "CN of Ow−Ow (R < 0.3 nm)" denotes the number of Ow within 0.3 nm from Ow; phase-separated states are denoted with filled diamonds (indicated in bold in the legend), while mixed states are plotted with unfilled circles. "H_2O-rich" and "CO_2-rich" phases indicate the water-rich phase and CO_2-rich phase in the slab system, respectively.

5 and S5−S7, while those for R = 0.5 nm are presented in Figures S8−S11. Additionally, in Figure S12, the mean ⟨CN⟩ and mode values of CN are plotted with respect to Δx_{CO_2}; the coexistence line of the CO_2-rich phase (see Figure 3) is defined as Δx_{CO_2} = 0% (see Table 2).

As x_{CO_2} increases, the CN of C−C (Figures S7 and S11) and Ow−C (Figures S5 and S9) increases while that of C−Ow (Figures S6 and S10) and Ow−Ow (Figures 5 and S8) decreases at all pressure and temperature conditions. As shown in Figures 5 and S8, the majority of the CN of Ow−Ow (R = 0.3 and 0.5 nm) becomes zero in the x_{CO_2} range where CO_2 and H_2O are in a mixed state under CO_2-rich conditions ($\Delta x_{CO_2} \geq 0\%$), indicating a strong correlation with the phase change. This characteristic feature was observed especially in R = 0.3 nm which corresponds to the first peak of Ow−Ow RDF of pure water (see Figure S4). The shift of the main broad peak of the histogram of CN (Ow−Ow) in Figure 5 by increasing x_{CO_2} would reflect the increase in the number of water molecules dissolving into the CO_2 phase, where they tend to become isolated from each other. By contrast, as shown in Figures S5−S7, S9−S11, and Figure S12, the other CNs—namely, C−Ow, Ow−C, and C−C—do not exhibit a pronounced correlation with the phase transition, indicating that they are less sensitive to the thermodynamic state of the system.

The CN histograms imply that it is insightful to shed light on the interaction and structural changes of water molecules in the phase transition. In the following subsection, the frequency distribution of hydrogen bond numbers is evaluated, focusing on the relationship between the structure and molecular interactions.

3.3. Hydrogen Bond. Distribution of n_{HB} for the CO_2 + water system at each temperature is presented in Figure 6. The legend in each graph indicates x_{CO_2}. Additionally, in Figure 7, the mean ⟨n_{HB}⟩ and mode values of n_{HB} are plotted with respect to Δx_{CO_2}, the difference from the coexistence line (CO_2-rich side) (see Table 2).

https://doi.org/10.1021/acsomega.4c00133
ACS Omega 2024, 9, 20976−20987

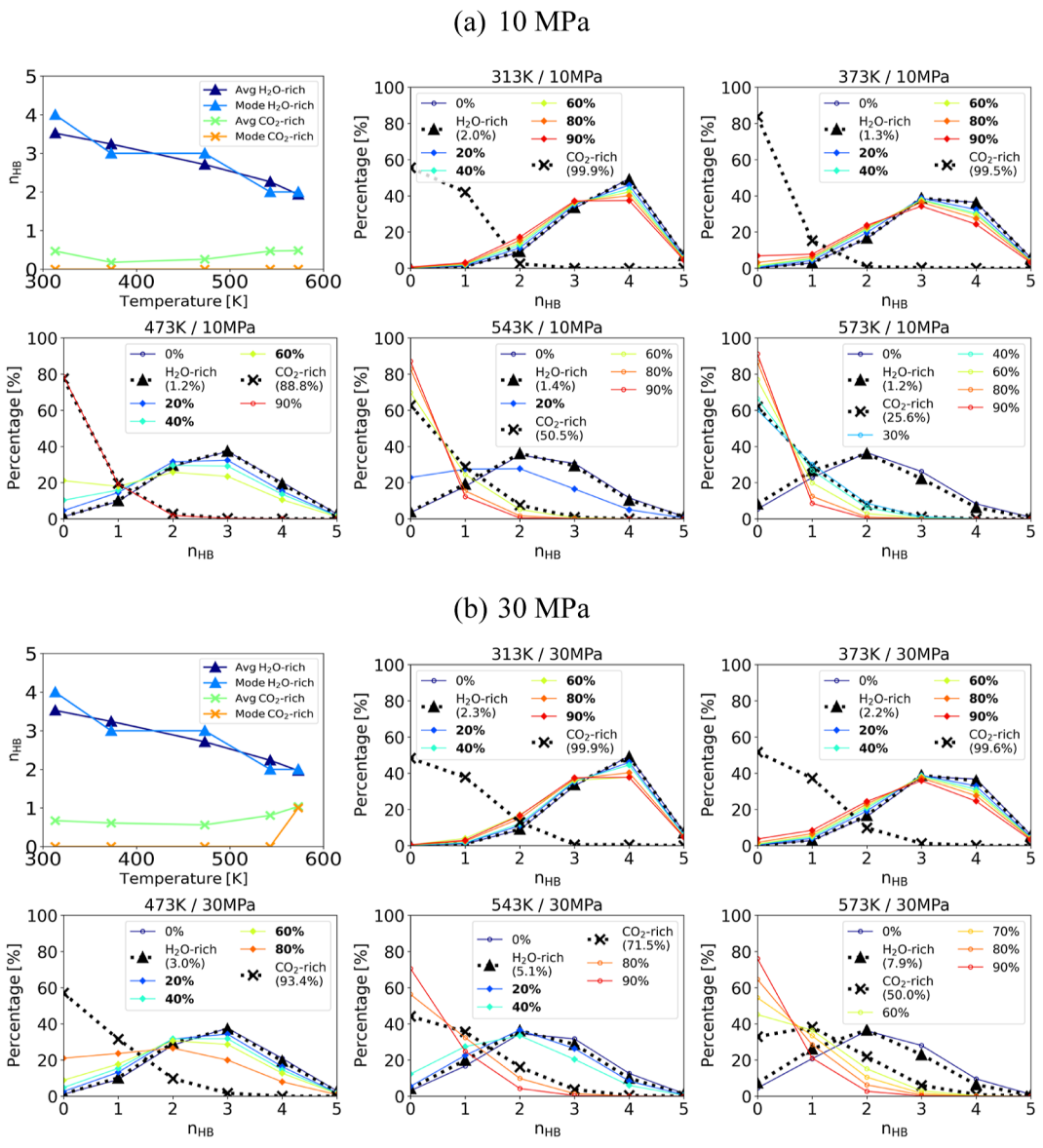

Figure 6. Number of hydrogen bonds per H_2O molecule at (a) 10 and (b) 30 MPa; phase-separated states are denoted with filled diamonds (indicated in bold in the legend), while mixed states are plotted with unfilled circles. "H_2O-rich" and "CO_2-rich" phases indicate the water-rich phase and CO_2-rich phase in the slab system, respectively.

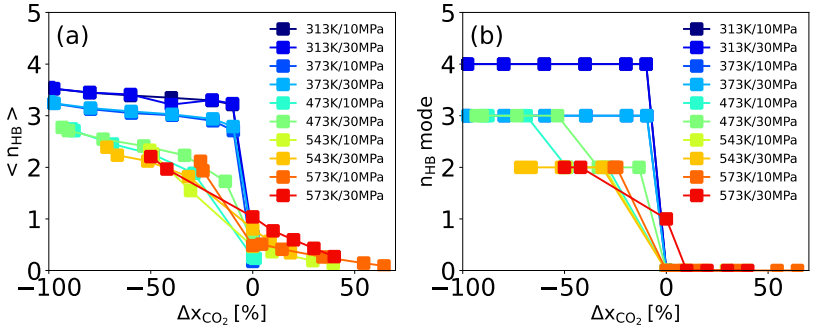

Figure 7. Mean $\langle n_{HB} \rangle$ (a) and mode (b) of n_{HB} with respect to Δx_{CO_2}, the difference from the coexistence line (CO_2-rich side).

Regarding the pure-water systems (x_{CO_2} = 0%), as shown in Figure 6, temperature increase leads to decrease in n_{HB} as already reported in previous experiments and molecular simulations.[62,75−77] As the temperature increases, the mode of n_{HB} tends to decrease; at 30 MPa, it is 4 at 313 K while it is 3 at 373 and 473 K. It is 2 at 543 and 573 K. At 10 MPa, n_{HB} decreases against temperature in a similar way to that at 30 MPa. Note that, concerning the definition of n_{HB} introduced in Section 2.4.2, n_{HB} calculated with an r_{DA} of 0.3 nm, which has also been used as a criterion in a previous study and an analysis

https://doi.org/10.1021/acsomega.4c00133
ACS Omega 2024, 9, 20976−20987

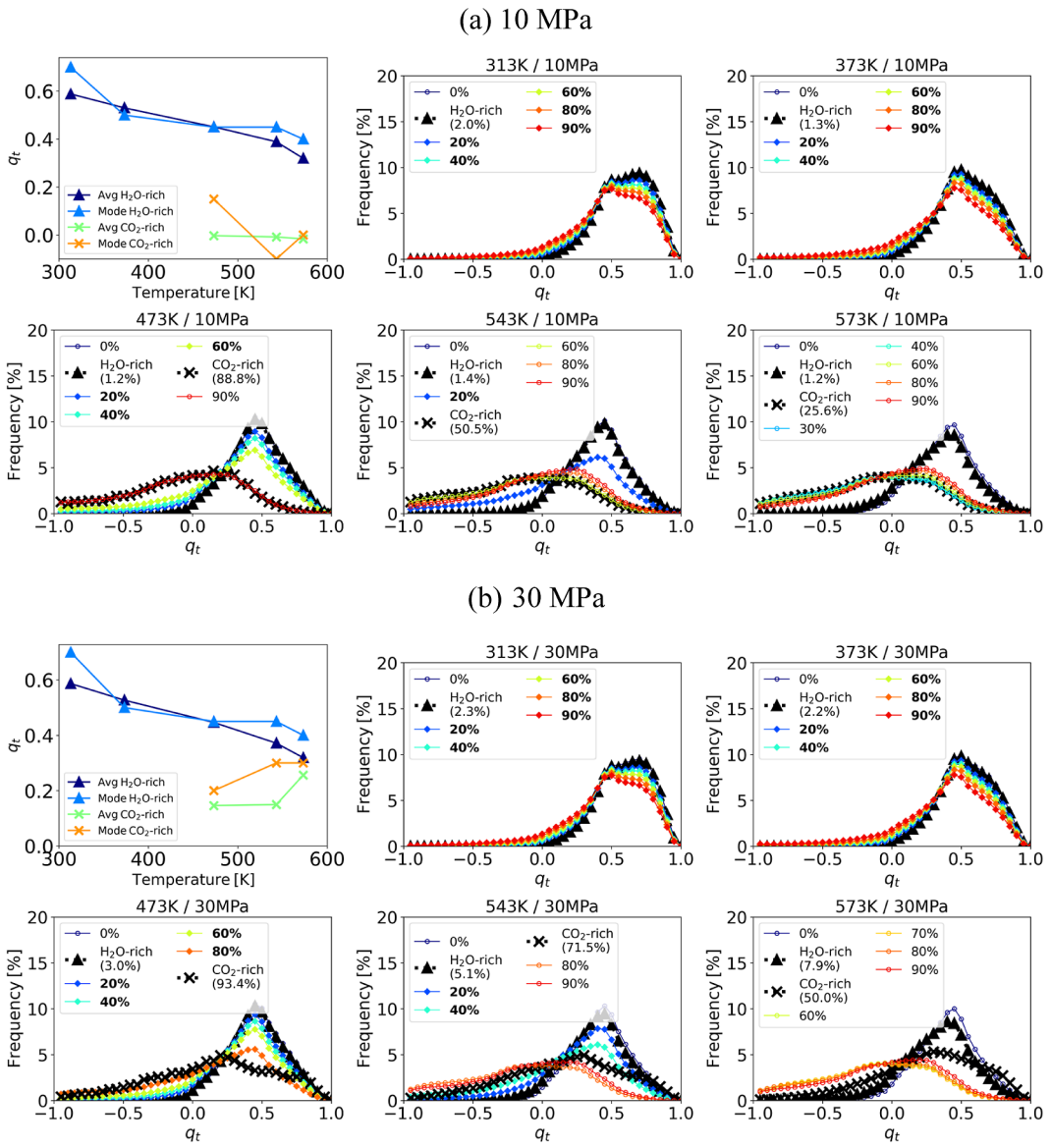

Figure 8. Tetrahedrality at (a) 10 and (b) 30 MPa; phase-separated states are denoted with filled diamonds (indicated in bold in the legend), while mixed states are plotted with unfilled circles. "H_2O-rich" and "CO_2-rich" phases indicate the water-rich phase and CO_2-rich phase in the slab system, respectively.

tool,[78] is also shown in Figure S13. Given the excellent reproducibility of n_{HB} of pure water in our calculations as well as previous molecular simulations,[62,75−77] r_{DA} = 0.35 nm is considered to be appropriate in our studied conditions.

Regarding x_{CO_2} > 0%, at 313 K under 10 and 30 MPa, the mode is 4 in most ranges of x_{CO_2}, and the majority of the water molecules have 3 to 4 hydrogen bonds. At 373 K under 10 and 30 MPa, the mode is 3 at x_{CO_2} from 10 to 90%.

Under temperature conditions for CO_2-EGS and CPG technology, at 473 K and 30 MPa, the mode is 2 or 3 and the majority of the water molecules have 1 to 4 hydrogen bonds in the range of x_{CO_2} from 10 to 80%. By contrast, at x_{CO_2} = 93.4% (Δx_{CO_2} = 0.0%, "CO_2 rich" in Figure 6b), the mode is 0, indicating that the majority of water molecules do not have any hydrogen bond. This drastic change is seen at x_{CO_2} = 88.8% (Δx_{CO_2} = 0.0%, "CO_2 rich" in Figure 6b) at 473 K and 10 MPa, which is consistent with the phase change shown in the $P-x$ diagram (Figure 3).

At 543 K and 30 MPa, the mode is 2 in the range of x_{CO_2} from 10 to 40% and is 0 at $x_{CO_2} \geq 71.5\%$ ($\Delta x_{CO_2} \geq 0.0\%$). A similar significant shift of the mode is seen between x_{CO_2} = 20% ($\Delta x_{CO_2} = -30.5\%$) and 50.5% ($\Delta x_{CO_2}$ = 0.0%) at 543 K and 10 MPa.

At 573 K and 30 MPa, the mode is 2 at the water-rich phase (x_{CO_2} = 7.9%) while the majority of water molecules exist as unbounded molecules (monomers) at $x_{CO_2} \geq 50\%$ ($\Delta x_{CO_2} \geq$ 0%). At 573 K and 10 MPa, the monomer is the majority of the form of water molecules under a broader range of x_{CO_2}. These results indicate that there is a strong correlation between the phase behavior and n_{HB}; the majority of water molecules become monomers in a mixed state. Moreover, from the perspective of mean values shown in Figure 7a, it is notable that in mixed systems, $\langle n_{HB} \rangle$ decreases to less than one,

https://doi.org/10.1021/acsomega.4c00133
ACS Omega 2024, 9, 20976−20987

representing a significant change. Furthermore, as the temperature increases, the difference in hydrogen bond numbers between water-rich and CO_2-rich phases lessens. Concurrently, according to our previous simulation study[29] performed using the LogMFD method,[79,80] the free-energy barrier that a H_2O molecule must overcome to permeate from the water-rich phase to the CO_2-rich phase diminishes by increasing temperature. Given that the number of hydrogen bonds is directly correlated with structural energy, these observations are consistent with each other from an energetic point of view. Moreover, as shown in Figure S14, the larger amount of hydrogen bonds is associated with CO_2 under higher temperature and x_{CO_2} conditions, especially in a mixed state. This provides us new insights into the structural properties of water in phase-separated and mixture systems. Hydrogen bonding plays a crucial role in characteristics of water such as surface tension[81] and viscosity;[33] therefore, our simulation data hold significant value for calibrating parameters in predictive models of transport properties, as well as for interpreting the alterations in the physical properties of CO_2 + H_2O systems attributable to phase transitions.

3.4. Tetrahedrality. Distribution of q_t for the CO_2 + H_2O system at 10 and 30 MPa is plotted in Figure 8a,b. The decreasing trend of the q_t mode of pure water (x_{CO_2} = 0%) was observed against the increasing temperature, which is consistent with a trend reported in previous molecular simulation studies.[30] This is also considered reasonable given that n_{HB} also decreases against temperature, leading to a decrease in structural orderliness.

Regarding x_{CO_2} > 0%, we observe significant peak shifts that seem to be related to the phase behavior, in addition to the changes of the overall profile of the q_t histogram with temperature. In the phase-separated state, marked by filled diamonds (bolded in the legend) in Figure 8, the mode of q_t was approximately 0.5 or higher. Conversely, in the mixed state, the mode of q_t was close to 0, and the peak was not as pronounced as that observed in the phase-separated state. For instance, at 473 K, the shift of the highest peak is notable from 60 to 88.8% (Δx_{CO_2} from −28.8 to 0.0%) at 10 MPa while it is prominent from 80 to 93.4% (Δx_{CO_2} from −13.4 to 0.0%) at 30 MPa, which is consistent with the phase transition shown in Figure 3. A similar clear change was observed at 543 K; the shape of the histogram varies near the phase separation condition. At 573 K, similar changes were observed, while the peak shift is more vague than lower temperature conditions. This can be attributed to the fact that at 10 MPa and 573 K, the orderliness is low even in the state of pure water, so the changes in q_t associated with the phase transition did not manifest significantly. At 573 K and 30 MPa, similar peak shifts to those at 573 K and 10 MPa are seen, as shown in Figure 8b.

Furthermore, the decomposition of q_t based on the CN with R = 0.35 nm for conditions of 313 K at 10 MPa and 543 K at 30 MPa is illustrated in Figure S15. At 313 K and 10 MPa, q_t exhibits higher values when the CN is 4, indicating a more ordered structure. By contrast, at 543 K and 30 MPa, even with a coordination of four oxygen atoms, the mode value dips below 0.5. This suggests a decline of the structural orderliness regardless of the CN. Notably, this trend is consistent across various CO_2 concentration, including cases with x_{CO_2} = 70 or 90% and even when x_{CO_2} = 0%. This indicates that the observed decrease in tetrahedrality and increase in randomness with rising temperatures are not limited to CO_2-rich environments but are also a characteristic of pure water systems under elevated temperatures.

This correspondence between changes of the mode of q_t and the phase transition of the CO_2 + H_2O systems was observed at all temperatures of 473, 543, and 573 K (note that no phase transition was observed from 10 to 90% at 313 and 373 K, as shown in Figure 3). q_t was significantly low when the majority of water molecules have no hydrogen bond, as seen in Figure 6; this is reasonable given that the tetrahedrality of water is relevant to the hydrogen bond network. The consistency between the descriptor q_t, which considers only water molecules, and n_{HB}, which also takes into account CO_2, suggests that the distinction between phase-separated and mixed states in the CO_2 + H_2O system can be well characterized by the structure of the water molecules.

4. CONCLUSIONS

In order to gain atomic-scale perspective of the phase behavior of CO_2 + H_2O systems, we performed MD simulations at temperature from 313 to 573 K, which includes promising reservoir conditions for CGS, CO_2-EGS, and CPG technology. The P−x diagram computed by the DC method is in good agreement with previous experiments and SAFT-based equations of state (simplified CPA, PC-SAFT, and SAFT-VR Mie models). Our results reproduced experimental data better than previous molecular simulation studies by using the same force fields. This has demonstrated that rigid models for CO_2 (EPM2, TraPPE, and PPL) and H_2O (SPC/E and TIP4P/2005) in conjunction with the DC method are promising tools to simulate phase behavior across a broad range of temperature and pressure conditions. Furthermore, our simulation setup described in detail could serve as useful benchmarks for phase behavior calculations.

Structural analysis clearly reveals correlations between the phase transition and variations in the structural orderliness of CO_2 + H_2O systems. Notably, the CN of Ow−Ow appears to be significantly tied to the phase transition. By contrast, other CNs such as CN (C−Ow), CN (Ow−C), and CN (C−C) do not show a marked correlation with the phase transition, suggesting that they are less sensitive to the thermodynamic state of the system. When CO_2 and H_2O are mixed, the majority of H_2O molecules do not have any hydrogen bond, existing predominantly in a monomeric state. This finding is further corroborated by the results of analyses focusing on tetrahedrality. The visualization of the phase behavior through snapshots will provide visual insights into these analytical results. In conditions where direct observation is challenging due to high temperatures, the value of such visualizations becomes even more pronounced.

This research enriches our atomic-scale understanding of the phase behavior in CO_2 + H_2O systems and offers crucial insights for interpreting lab-scale experiments and calibrating parameters in field-scale reservoir simulations more accurately. For instance, the data regarding the number of hydrogen bonds could be extensively employed in both modeling and understanding of thermodynamic properties and transport coefficients in the CO_2 + H_2O mixtures. Furthermore, the present findings would be valuable for guiding promising future studies, which include the estimation of the mobility of CO_2 + H_2O mixtures and the wettability of water vs CO_2 on prevalent mineral surfaces. These factors are considered to be

https://doi.org/10.1021/acsomega.4c00133
ACS Omega 2024, 9, 20976−20987

key contributors to the efficiency of CGS, CO_2-EGS, and CPG technology.

■ ASSOCIATED CONTENT

Supporting Information

The Supporting Information is available free of charge at https://pubs.acs.org/doi/10.1021/acsomega.4c00133.

> Number of molecules in the slab systems (Table S1); LJ cross parameters (Table S2); box size of DC simulation systems (Table S3); box size of the cubic systems (Table S4); averaged pressure of the cubic systems (Table S5); time variation of P_{zz} in the production run of DC calculations (Figure S1); time variation of the mole fraction x_{CO_2} in the CO_2-rich phase (Figure S2); RDF of C−C at 10 MPa and 30 MPa (Figure S3); RDF of Ow−Ow at 10 MPa and 30 MPa (Figure S4); coordination numbers of Ow−C, C−Ow, and C−C at R < 0.3 nm (Figures S5−S7); coordination numbers of Ow−Ow, Ow−C, C−Ow, and C−C at R < 0.5 nm (Figures S8−S11); mean ⟨CN⟩ and mode of CN with respect to Δx_{CO_2} (Figure S12); number of hydrogen bonds per H_2O molecule at 10 MPa and 30 MPa (Figure S13); percentage of hydrogen bond by CO_2 (Figure S14); and frequency distribution of tetrahedrality (Figure S15) (PDF)

■ AUTHOR INFORMATION

Corresponding Authors

Masashige Shiga − *Geological Survey of Japan, National Institute of Advanced Industrial Science and Technology (AIST), Tsukuba, Ibaraki 305-8567, Japan;* orcid.org/0000-0002-8577-3402; Email: m.shiga@aist.go.jp

Tetsuya Morishita − *Research Center for Computational Design of Advanced Functional Materials (CD-FMat), National Institute of Advanced Industrial Science and Technology (AIST), Tsukuba, Ibaraki 305-8568, Japan;* orcid.org/0000-0002-8308-6211; Phone: +81-90-5465-7285; Email: t-morishita@aist.go.jp

Authors

Naoki Nishiyama − *Geological Survey of Japan, National Institute of Advanced Industrial Science and Technology (AIST), Tsukuba, Ibaraki 305-8567, Japan*

Masao Sorai − *Geological Survey of Japan, National Institute of Advanced Industrial Science and Technology (AIST), Tsukuba, Ibaraki 305-8567, Japan*

Masaatsu Aichi − *Department of Environment Systems, Graduate School of Frontier Sciences, The University of Tokyo, Kashiwa, Chiba 277-8563, Japan*

Ayaka Abe − *Japan Organization for Metals and Energy Security (JOGMEC), Tokyo 105-0001, Japan;* Present Address: Geological Survey of Japan, National Institute of Advanced Industrial Science and Technology (AIST), Tsukuba, Ibaraki 305-8567, Japan

Complete contact information is available at: https://pubs.acs.org/10.1021/acsomega.4c00133

Notes

The authors declare no competing financial interest.

■ ACKNOWLEDGMENTS

This work was supported by a fund for the project "Carbon recycle CO_2 geothermal power generation technology" from the Japan Organization for Metals and Energy Security (JOGMEC). T.M. was partly supported by a Grant-in-Aid for Scientific Research from JSPS KAKENHI (grant no. 22K03564). Simulations were performed using the computing resources offered under the category of General Projects by the Research Institute for Information Technology, Kyushu University.

■ REFERENCES

(1) IEA. *CCUS*; IEA: Paris, 2023. https://www.iea.org/reports/ccus, License: CC BY 4.0.

(2) Li, N.; Feng, W.; Yu, J.; Chen, F.; Zhang, Q.; Zhu, S.; Hu, Y.; Li, Y. Recent Advances in Geological Storage: Trapping Mechanisms, Storage Sites, Projects, and Application of Machine Learning. *Energy Fuels* **2023**, *37* (14), 10087−10111.

(3) Kumar, Y.; Sangwai, J. S. A Perspective on the Effect of Physicochemical Parameters, Macroscopic Environment, Additives, and Economics to Harness the Large-Scale Hydrate-Based CO_2 Sequestration Potential in Oceans. *ACS Sustain. Chem. Eng.* **2023**, *11* (30), 10950−10979.

(4) Brown, D. W. A Hot Dry Rock Geothermal Energy Concept Utilizing Supercritical CO_2 Instead of Water. In *Proceedings of the Twenty-fifth Workshop on Geothermal Reservoir Engineering*; Stanford University, 2000; pp 233−238.

(5) Esteves, A. F.; Santos, F. M.; Magalhães Pires, J. C. Carbon Dioxide as Geothermal Working Fluid: An Overview. *Renewable Sustainable Energy Rev.* **2019**, *114*, 109331.

(6) Pruess, K. On Production Behavior of Enhanced Geothermal Systems with CO_2 as Working Fluid. *Energy Convers. Manage.* **2008**, *49* (6), 1446−1454.

(7) Avanthi Isaka, B.; Ranjith, P. G.; Rathnaweera, T. D. The Use of Super-Critical Carbon Dioxide as the Working Fluid in Enhanced Geothermal Systems (EGSs): A Review Study. *Sustain. Energy Technol. Assessments* **2019**, *36*, 100547.

(8) Ishida, T.; Aoyagi, K.; Niwa, T.; Chen, Y.; Murata, S.; Chen, Q.; Nakayama, Y. Acoustic Emission Monitoring of Hydraulic Fracturing Laboratory Experiment with Supercritical and Liquid CO_2. *Geophys. Res. Lett.* **2012**, *39*(16)..

(9) Ishida, T.; Chen, Y.; Bennour, Z.; Yamashita, H.; Inui, S.; Nagaya, Y.; Naoi, M.; Chen, Q.; Nakayama, Y.; Nagano, Y. Features of CO_2 Fracturing Deduced from Acoustic Emission and Microscopy in Laboratory Experiments. *J. Geophys. Res.: Solid Earth* **2016**, *121* (11), 8080−8098.

(10) Pruess, K. Enhanced Geothermal Systems (EGS) Using CO_2 as Working Fluid—A Novel Approach for Generating Renewable Energy with Simultaneous Sequestration of Carbon. *Geothermics* **2006**, *35* (4), 351−367.

(11) Wu, Y.; Li, P. The Potential of Coupled Carbon Storage and Geothermal Extraction in a CO_2-Enhanced Geothermal System: A Review. *Geoth. Energy* **2020**, *8* (1), 19.

(12) Song, W.; Wang, C.; Du, Y.; Shen, B.; Chen, S.; Jiang, Y. Comparative Analysis on the Heat Transfer Efficiency of Supercritical CO_2 and H_2O in the Production Well of Enhanced Geothermal System. *Energy* **2020**, *205*, 118071.

(13) Canbaz, C. H.; Ekren, O.; Aksoy, N. Review of Wellbore Flow Modelling in CO_2-Bearing Geothermal Reservoirs. *Geothermics* **2022**, *98*, 102284.

(14) Zhong, C.; Xu, T.; Gherardi, F.; Yuan, Y. Comparison of CO_2 and Water as Working Fluids for an Enhanced Geothermal System in the Gonghe Basin, Northwest China. *Gondwana Res.* **2023**, *122*, 199−214.

(15) Croucher, A.; O'Sullivan, J.; Yeh, A.; O'Sullivan, M. Benchmarking and Experiments with Waiwera, a New Geothermal

Simulator. In *Proc. 43rd Workshop on Geothermal Reservoir Engineering*; Stanford University: Stanford, California, USA, 2018.
(16) Masuoka, K.; Yamamoto, H.; Kumamoto, S. Simulation Study on Heat Extraction Efficiency and CO_2 Recovery Rate for CO_2-EGS in Hydrothermal Reservoirs. In *Proceedings, 48th Workshop on Geothermal Reservoir Engineering*, 2023.
(17) Tödheide, K.; Franck, E. U. Das Zweiphasengebiet und die Kritische Kurve im System Kohlendioxid-Wasser bis zu Drucken von 3500 bar. *Z. Phys. Chem.* **1963**, *37* (5_6), 387−401.
(18) Takenouchi, S.; Kennedy, G. C. The Binary System H_2O-CO_2 at High Temperatures and Pressures. *Am. J. Sci.* **1964**, *262* (9), 1055−1074.
(19) Kontogeorgis, G. M.; Michelsen, M. L.; Folas, G. K.; Derawi, S.; Von Solms, N.; Stenby, E. H. Ten Years with the CPA (Cubic-Plus-Association) Equation of State. Part 1. Pure Compounds and Self-Associating Systems. *Ind. Eng. Chem. Res.* **2006**, *45* (14), 4855−4868.
(20) Gross, J.; Sadowski, G. Application of the Perturbed-Chain SAFT Equation of State to Associating Systems. *Ind. Eng. Chem. Res.* **2002**, *41* (22), 5510−5515.
(21) Dufal, S.; Lafitte, T.; Galindo, A.; Jackson, G.; Haslam, A. J. Developing Intermolecular-Potential Models for Use with the SAFT-VR M ie Equation of State. *AIChE J.* **2015**, *61* (9), 2891−2912.
(22) Valtz, A.; Chapoy, A.; Coquelet, C.; Paricaud, P.; Richon, D. Vapour-Liquid Equilibria in the Carbon Dioxide-Water System, Measurement and Modelling from 278.2 to 318.2 K. *Fluid Phase Equilib.* **2004**, *226*, 333−344.
(23) Chabab, S.; Théveneau, P.; Corvisier, J.; Coquelet, C.; Paricaud, P.; Houriez, C.; Ahmar, E. E. Thermodynamic Study of the CO_2-H_2O-NaCl System: Measurements of CO_2 Solubility and Modeling of Phase Equilibria Using Soreide and Whitson, Electrolyte CPA and SIT Models. *Int. J. Greenhouse Gas Control* **2019**, *91*, 102825.
(24) da Rocha, S. R. P.; Johnston, K. P.; Westacott, R. E.; Rossky, P. J. Molecular Structure of the Water-Supercritical CO_2 Interface. *J. Phys. Chem. B* **2001**, *105*, 12092−12104.
(25) Zhao, L.; Lin, S.; Mendenhall, J. D.; Yuet, P. K.; Blankschtein, D. Molecular Dynamics Investigation of the Various Atomic Force Contributions to the Interfacial Tension at the Supercritical CO_2-Water Interface. *J. Phys. Chem. B* **2011**, *115*, 6076−6087.
(26) Nielsen, L. C.; Bourg, I. C.; Sposito, G. Predicting CO_2-Water Interfacial Tension Under Pressure and Temperature Conditions of Geologic CO_2 Storage. *Geochim. Cosmochim. Acta* **2012**, *81*, 28−38.
(27) Zhao, L.; Ji, J.; Tao, L.; Lin, S. Ionic Effects on Supercritical CO_2-Brine Interfacial Tensions: Molecular Dynamics Simulations and a Universal Correlation with Ionic Strength, Temperature, and Pressure. *Langmuir* **2016**, *32*, 9188−9196.
(28) Naeiji, P.; Woo, T. K.; Alavi, S.; Ohmura, R. Molecular Dynamics Simulations of Interfacial Properties of the CO_2-Water and CO_2-CH_4-Water Systems. *J. Chem. Phys.* **2020**, *153*, 044701.
(29) Shiga, M.; Morishita, T.; Sorai, M. Interfacial Tension of Carbon Dioxide-Water Under Conditions of CO_2 Geological Storage and Enhanced Geothermal Systems: A Molecular Dynamics Study on the Effect of Temperature. *Fuel* **2023**, *337*, 127219.
(30) Errington, J. R.; Debenedetti, P. G. Relationship Between Structural Order and the Anomalies of Liquid Water. *Nature* **2001**, *409* (6818), 318−321.
(31) Morishita, T. Anomalous Diffusivity in Supercooled Liquid Silicon Under Pressure. *Phys. Rev. E* **2005**, *72* (2), 021201.
(32) Morishita, T. Structural and Dynamical Heterogeneity in Deeply Supercooled Liquid Silicon. *Phys. Rev. E* **2008**, *77* (2), 020501.
(33) Marcus, Y. On Transport Properties of Hot Liquid and Supercritical Water and Their Relationship to the Hydrogen Bonding. *Fluid Phase Equilib.* **1999**, *164* (1), 131−142.
(34) Scheiner, B.; Yoon, T. J. Calculation of Self-Diffusion Coefficients in Supercritical Carbon Dioxide Using Mean Force Kinetic Theory. *J. Chem. Phys.* **2021**, *154* (13), 134101.
(35) Xie, M.; Zhang, M.; Jin, Z. Machine Learning-Based Interfacial Tension Equations for (H2+ CO_2)-Water/Brine Systems over a Wide Range of Temperature and Pressure. *Langmuir* **2024**, *40*, 5369−5377.
(36) Oparin, R.; Tassaing, T.; Danten, Y.; Besnard, M. A Vibrational Spectroscopic Study of Structure Evolution of Water Dissolved in Supercritical Carbon Dioxide Under Isobaric Heating. *J. Chem. Phys.* **2004**, *120* (22), 10691−10698.
(37) Oparin, R.; Tassaing, T.; Danten, Y.; Besnard, M. Water-Carbon Dioxide Mixtures at High Temperatures and Pressures: Local Order in the Water Rich Phase Investigated by Vibrational Spectroscopy. *J. Chem. Phys.* **2005**, *123* (22), 224501.
(38) Liu, Y.; Panagiotopoulos, A. Z.; Debenedetti, P. G. Monte Carlo Simulations of High-Pressure Phase Equilibria of CO_2-H_2O Mixtures. *J. Phys. Chem. B* **2011**, *115* (20), 6629−6635.
(39) Vlcek, L.; Chialvo, A. A.; Cole, D. R. Optimized Unlike-Pair Interactions for Water-Carbon Dioxide Mixtures Described by the SPC/E and EPM2Models. *J. Phys. Chem. B* **2011**, *115* (27), 8775−8784.
(40) Orozco, G. A.; Economou, I. G.; Panagiotopoulos, A. Z. Optimization of Intermolecular Potential Parameters for the CO_2/H_2O Mixture. *J. Phys. Chem. B* **2014**, *118* (39), 11504−11511.
(41) Jiang, H.; Economou, I. G.; Panagiotopoulos, A. Z. Phase Equilibria of Water/CO_2 and Water/n-Alkane Mixtures from Polarizable Models. *J. Phys. Chem. B* **2017**, *121* (6), 1386−1395.
(42) Vega, C.; de Miguel, E. Surface Tension of the Most Popular Models of Water by Using the Test-Area Simulation Method. *J. Chem. Phys.* **2007**, *126* (15), 154707.
(43) Sakamaki, R.; Sum, A. K.; Narumi, T.; Yasuoka, K. Molecular Dynamics Simulations of Vapor/Liquid Coexistence Using the Nonpolarizable Water Models. *J. Chem. Phys.* **2011**, *134* (12), 124708.
(44) Espinosa, J. R.; Young, J. M.; Jiang, H.; Gupta, D.; Vega, C.; Sanz, E.; Debenedetti, P. G.; Panagiotopoulos, A. Z. On the Calculation of Solubilities via Direct Coexistence Simulations: Investigation of NaCl Aqueous Solutions and Lennard-Jones Binary Mixtures. *J. Chem. Phys.* **2016**, *145* (15), 154111.
(45) van Rooijen, W. A.; Habibi, P.; Xu, K.; Dey, P.; Vlugt, T. J. H.; Hajibeygi, H.; Moultos, O. A. Interfacial Tensions, Solubilities, and Transport Properties of the H2/H_2O/NaCl System: A Molecular Simulation Study. *J. Chem. Eng. Data* **2023**, *69*, 307−319.
(46) Panagiotopoulos, A. Z. Direct Determination of Fluid Phase Equilibria by Simulation in the Gibbs Ensemble: A Review. *Mol. Simul.* **1992**, *9* (1), 1−23.
(47) Li, W.; Nan, Y.; Zhang, Z.; You, Q.; Jin, Z. Hydrophilicity/Hydrophobicity Driven CO_2 Solubility in Kaolinite Nanopores in Relation to Carbon Sequestration. *Chem. Eng. J.* **2020**, *398*, 125449.
(48) Hosseinzadeh Dehaghani, Y.; Assareh, M.; Feyzi, F. Simultaneous Prediction of Equilibrium, Interfacial, and Transport Properties of CO_2-Brine Systems Using Molecular Dynamics Simulation: Applications to CO_2 Storage. *Ind. Eng. Chem. Res.* **2022**, *61* (41), 15390−15406.
(49) Harris, J. G.; Yung, K. H. Carbon Dioxide's Liquid-Vapor Coexistence Curve and Critical Properties as Predicted by a Simple Molecular Model. *J. Phys. Chem.* **1995**, *99* (31), 12021−12024.
(50) Potoff, J. J.; Siepmann, J. I. Vapor-Liquid Equilibria of Mixtures Containing Alkanes, Carbon Dioxide, and Nitrogen. *AIChE J.* **2001**, *47* (7), 1676−1682.
(51) Berendsen, H. J. C.; Grigera, J. R.; Straatsma, T. P. The Missing Term in Effective Pair Potentials. *J. Phys. Chem.* **1987**, *91* (24), 6269−6271.
(52) Abascal, J. L.; Vega, C. A General Purpose Model for the Condensed Phases of Water: TIP4P/2005. *J. Chem. Phys.* **2005**, *123* (23), 234505.
(53) Patterson, M. I. H. P. C.; Lynden-Bell, R. M. A Molecular Dynamics Study of Carbon Dioxide in Water: Diffusion, Structure, and Thermodynamics. *Mol. Phys.* **1998**, *94* (6), 963−972.
(54) Hess, B.; Bekker, H.; Berendsen, H. J.; Fraaije, J. G. LINCS: A Linear Constraint Solver for Molecular Simulations. *J. Comput. Chem.* **1997**, *18* (12), 1463−1472.

https://doi.org/10.1021/acsomega.4c00133
ACS Omega 2024, 9, 20976−20987

(55) Van Der Spoel, D.; Lindahl, E.; Hess, B.; Groenhof, G.; Mark, A. E.; Berendsen, H. J. GROMACS: Fast, Flexible, and Free. *J. Comput. Chem.* **2005**, *26* (16), 1701−1718.
(56) Humphrey, W.; Dalke, A.; Schulten, K. VMD: Visual Molecular Dynamics. *J. Mol. Graphics* **1996**, *14* (1), 33−38.
(57) Nosé, S. A Molecular Dynamics Method for Simulations in the Canonical Ensemble. *Mol. Phys.* **1984**, *52* (2), 255−268.
(58) Hoover, W. G. Canonical Dynamics: Equilibrium Phase-Space Distributions. *Phys. Rev. A* **1985**, *31* (3), 1695−1697.
(59) Berendsen, H. J.; Postma, J. P. M.; van Gunsteren, W. F.; DiNola, A. R. H. J.; Haak, J. R. Molecular Dynamics with Coupling to an External Bath. *J. Chem. Phys.* **1984**, *81* (8), 3684−3690.
(60) Parrinello, M.; Rahman, A. Polymorphic Transitions in Single Crystals: A New Molecular Dynamics Method. *J. Appl. Phys.* **1981**, *52* (12), 7182−7190.
(61) Regy, R. M.; Dignon, G. L.; Zheng, W.; Kim, Y. C.; Mittal, J. Sequence Dependent Phase Separation of Protein-Polynucleotide Mixtures Elucidated Using Molecular Simulations. *Nucleic Acids Res.* **2020**, *48* (22), 12593−12603.
(62) Karalis, K.; Ludwig, C.; Niceno, B. Supercritical Water Anomalies in the Vicinity of the Widom Line. *Sci. Rep.* **2019**, *9* (1), 15731.
(63) Luzar, A.; Chandler, D. Hydrogen-Bond Kinetics in Liquid Water. *Nature* **1996**, *379* (6560), 55−57.
(64) Morishita, T. How Does Tetrahedral Structure Grow in Liquid Silicon Upon Supercooling? *Phys. Rev. Lett.* **2006**, *97* (16), 165502.
(65) Wang, Z.; Zhou, Q.; Guo, H.; Yang, P.; Lu, W. Determination of Water Solubility in Supercritical CO_2 from 313.15 to 473.15 K and from 10 to 50 MPa by In-Situ Quantitative Raman Spectroscopy. *Fluid Phase Equilib.* **2018**, *476*, 170−178.
(66) Wiebe, R.; Gaddy, V. L. The Solubility in Water of Carbon Dioxide at 50, 75 and 100°, at Pressures to 700 Atmospheres. *J. Am. Chem. Soc.* **1939**, *61* (2), 315−318.
(67) Capobianco, R.; Gruszkiewicz, M. S.; Wesolowski, D. J.; Cole, D. R.; Bodnar, R. J. Vol.tric Properties and Fluid Phase Equilibria of CO_2+ H_2O. In *Proceedings, Thirty-Eighth Workshop on Geothermal Reservoir Engineering*; Stanford University: Stanford, CA, 2013; Vol. *38*.
(68) Duan, Z.; Sun, R. An Improved Model Calculating CO_2 Solubility in Pure Water and Aqueous NaCl Solutions from 273 to 533 K and from 0 to 2000 bar. *Chem. Geol.* **2003**, *193* (3−4), 257−271.
(69) Walker, P. J.; Yew, H. W.; Riedemann, A. Clapeyron. jl: An Extensible, Open-Source Fluid Thermodynamics Toolkit. *Ind. Eng. Chem. Res.* **2022**, *61* (20), 7130−7153.
(70) Cygan, R. T.; Liang, J. J.; Kalinichev, A. G. Molecular Models of Hydroxide, Oxyhydroxide, and Clay Phases and the Development of a General Force Field. *J. Phys. Chem. B* **2004**, *108* (4), 1255−1266.
(71) Javanbakht, G.; Sedghi, M.; Welch, W.; Goual, L. Molecular Dynamics Simulations of CO_2/Water/Quartz Interfacial Properties: Impact of CO_2 Dissolution in Water. *Langmuir* **2015**, *31* (21), 5812−5819.
(72) Tsimpanogiannis, I. N.; Moultos, O. A.; Franco, L. F.; Spera, M. B. D. M.; Erdős, M.; Economou, I. G. Self-Diffusion Coefficient of Bulk and Confined Water: A Critical Review of Classical Molecular Simulation Studies. *Mol. Simul.* **2019**, *45* (4−5), 425−453.
(73) Wang, H. D.; Chen, Y.; Ma, G. W. Effects of Capillary Pressures on Two-Phase Flow of Immiscible Carbon Dioxide Enhanced Oil Recovery in Fractured Media. *Energy* **2020**, *190*, 116445.
(74) Chen, Y.; Mao, Y.; Yang, L.; Wei, W.; Meng, Q.; Cai, J. A Comprehensive Review of Factors Affecting Dynamic Capillary Effect in Two-Phase Flow. *Transp. Porous Media* **2022**, *144* (1), 33−54.
(75) Gorbaty, Y. E.; Demianets, Y. N. The pair-correl.Ation functions of water at a pressure of 1 000 bar in the temperature range 25−500°C. *Chem. Phys. Lett.* **1983**, *100* (5), 450−454.
(76) Kalinichev, A. G.; Bass, J. D. Hydrogen Bonding in Supercritical Water. 2. Computer Simulations. *J. Phys. Chem. A* **1997**, *101* (50), 9720−9727.
(77) Dubey, V.; Erimban, S.; Indra, S.; Daschakraborty, S. Understanding the Origin of the Breakdown of the Stokes-Einstein Relation in Supercooled Water at Different Temperature-Pressure Conditions. *J. Phys. Chem. B* **2019**, *123* (47), 10089−10099.
(78) Gowers, R. J.; Linke, M.; Barnoud, J.; Reddy, T. J. E.; Melo, M. N.; Seyler, S. L.; Domanski, J.; Dotson, D. L.; Buchoux, S.; Kenney, I. M.; Beckstein, O. MDAnalysis: A Python Package for the Rapid Analysis of Molecular Dynamics Simulations. In *Proceedings of the 15th Python in Science Conference*, 2019. LA-UR-19−29136.
(79) Morishita, T.; Itoh, S. G.; Okumura, H.; Mikami, M. Free-Energy Calculation via Mean-Force Dynamics Using a Logarithmic Energy Landscape. *Phys. Rev. E* **2012**, *85* (6), 066702.
(80) Morishita, T.; Yonezawa, Y.; Ito, A. M. Free Energy Reconstruction from Logarithmic Mean-Force Dynamics Using Multiple Nonequilibrium Trajectories. *J. Chem. Theory Comput.* **2017**, *13* (7), 3106−3119.
(81) Hauner, I. M.; Deblais, A.; Beattie, J. K.; Kellay, H.; Bonn, D. The Dynamic Surface Tension of Water. *J. Phys. Chem. Lett.* **2017**, *8* (7), 1599−1603.

https://doi.org/10.1021/acsomega.4c00133
ACS Omega 2024, 9, 20976−20987